Role of intra-domain heterogeneity on ion and polymer dynamics in block polymer electrolytes: An approach for spatially resolving dynamics and ion transport

Priyanka M. Ketkar,[a] Nicholas F. Pietra,[b] Andrew G. Korovich,[b] Louis A. Madsen,[b,] and Thomas H. Epps, III[a,c,d,*]*

[a]Department of Chemical & Biomolecular Engineering, University of Delaware, Newark, Delaware 19716, United States

[b]Department of Chemistry and Macromolecules Innovation Institute, Virginia Polytechnic Institute and State University, Blacksburg, Virginia 24061, United States

[c]Department of Materials Science & Engineering, University of Delaware, Newark, Delaware 19716, United States

[d]Center for Research in Soft matter & Polymers (CRiSP), University of Delaware, Newark, Delaware 19716, United States

For Table of Contents Use Only

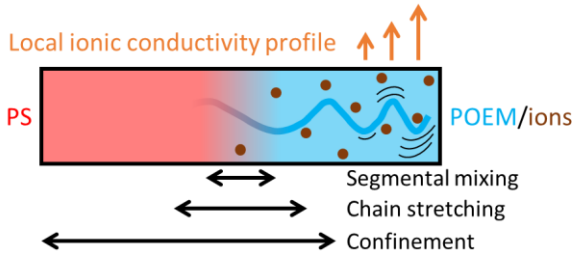

ABSTRACT

The design of safe and high-performance, nanostructured, block polymer (BP) electrolytes for lithium-ion batteries requires a thorough understanding of the key parameters that govern local structure and dynamics. Yet, the interfaces between microphase-separated domains can introduce complexities in this local behavior that can be challenging to quantify. Herein, the local polymer, cation (Li^+), and anion dynamics were described in salt-doped polystyrene-*block*-poly(*oligo*-oxyethylene methyl ether methacrylate) (PS-*b*-POEM) through a quantitative framework that considered the effects of polymer architecture, segmental mixing, chain stretching, and confinement on polymer mobility and ion transport. This framework was validated through nuclear magnetic resonance (NMR) spectroscopy measurements on solid (dry) polymer electrolyte samples. Notably, a mobility transition temperature ($T_{mobility}$) was identified through NMR spectroscopy that captured the local dynamics more accurately than the thermal glass transition temperature. Additionally, the approach quantitatively described the mobility gradient across a domain when segmental mixing effects were combined with chain stretching and confinement information, especially at higher segregation strengths – facilitating the assessment of local ion diffusion and conductivity. Spatially averaged local ion diffusion predictions quantitatively matched NMR-measured ion diffusivities in the BP samples, while spatially summed ionic

conductivity predictions across a domain qualitatively captured trends in the measured ionic conductivities.

INTRODUCTION

Nanostructured block polymer (BP) electrolytes provide a route to simultaneously tackle the safety and performance limitations that hamper lithium-ion batteries containing liquid electrolytes.[1-5] However, the presence of interfaces between microphase-separated domains results in nanoscale heterogeneities in structure and dynamics, such that transport near the interfaces often is compromised because of reduced segmental motion and ion solvation in the conducting mesophase.[6-11] There has been recent interest in tuning monomer-segment/ion distributions and local chain stretching (*i.e.*, the intra-domain composition and chain conformations) to achieve improved transport.[12] For example, tapered BPs, which have gradient monomer-segment composition profiles between homogeneous blocks, were used to tune intra-domain composition and chain conformations.[13-15] These tapered systems achieved significant increases in ionic conductivity relative to non-tapered BPs with comparable molecular weight, chemistry, and morphology.[13] Similarly, the blending of large-molecular-weight conducting homopolymers (HPs) into BPs formed local HP-rich channels within the conducting domain that improved transport.[16] The precise application of these concepts (*i.e.*, tapered BPs, BP/HP blends) in the efficient design of nanostructured electrolytes requires a thorough understanding of both the local ion transport across a mesophase and the key parameters that contribute to local structure and dynamics.

Several approaches have been used to elucidate local composition and dynamics in phase-separated polymer systems. For example, scattering and microscopy have been employed to probe the distributions of monomer segments and ions in nanostructured systems and visualize local

viscoelastic dynamics,[15, 17-20] while fluorescence spectroscopy measurements on tagged polymer samples have enabled the isolation and quantification of the effects of chain connectivity, segmental mixing, and confinement on the local glass transition temperature (T_g) within a self-assembled BP domain.[7, 21] Relative to experiments, simulations have provided a faster route (that eliminates potentially challenging sample preparation) to uncover how the degree of polymerization (N), Flory-Huggins interaction parameter (χ), monomer-segment composition profile, and monomer-segment friction factor contrast impact local chain conformations, monomer-segment distributions, ion solvation, ion distributions, and dynamics.[10, 11, 14, 22-27]

However, some challenges remain in the characterization of local polymer electrolyte dynamics. Scattering and microscopy methods that probe polymer dynamics are often limited to materials in which high local contrast (between different atoms, functional groups, or phases) can be achieved; this constraint can be prohibitive in many organic polymer systems.[28] Although staining and deuteration, for example, have been used to impart greater contrast in organic materials, there also is a risk of altering a material's meso/nanostructure.[29-32] Fluorescence spectroscopy measurements provide a precise experimental method to gauge local dynamics even in materials with low inherent scattering contrast, but this approach typically requires the synthesis of a large library of polymers to achieve sufficient data on local dynamics throughout a domain.[7] Moreover, the precise placement of fluorescent tags at targeted locations on a polymer chain necessitates a highly controlled synthetic scheme, such as ionic polymerization, which can exclude several common polymer chemistries and designs. In addition to quantifying polymer dynamics in electrolytes, it is also necessary to probe ion motion directly, as potential differences between ion and monomer-segment distributions[33, 34] may render inferences from polymer dynamics inaccurate.[10] Probing ion dynamics directly can be difficult *via* fluorescent tagging, scattering, and

microscopy. Furthermore, although simulations can overcome contrast-related challenges and can capture polymer and ion dynamics separately, these simulation results do not always provide quantitative matches to experimental data.[23, 35, 36] To address these challenges, a different approach to probe both local polymer and ion dynamics is reported herein.

In this study, a quantitative framework was developed predict local polymer mobility and ion transport across a domain in polystyrene-*block*-poly(*oligo*-oxyethylene methyl ether methacrylate) (PS-*b*-POEM) electrolytes. To obtain these predictions, monomer-segment and ion distributions across a domain were determined using the interfacial width between conducting and non-conducting mesophases and the volume fractions of these mesophases. Next, local transition temperatures (*e.g.*, local T_gs) across the domain were estimated *via* knowledge of the monomer-segment distributions described above, self-concentration of the monomer segments,[37] and bulk transition temperatures of the mesophases (inferred from equivalent HP samples). Then, local cation (Li^+) and anion diffusivities were calculated using the local transition temperatures and ion diffusivities in equivalent POEM HPs. Finally, upper-bound approximations for local ionic conductivities were made using the local ion diffusivities *via* the Nernst-Einstein equation.[38] Two different types of interfacial widths were investigated as input parameters: one obtained from small-angle X-ray scattering (SAXS) measurements that primarily captured segmental mixing and one gleaned from differential scanning calorimetry (DSC) data that likely encompassed chain stretching and confinement in addition to segmental mixing. Similarly, two types of HP transition temperature input parameters were studied: a T_g from DSC data and a mobility transition temperature ($T_{mobility}$) from nuclear magnetic resonance (NMR) spectroscopy measurements on solid (dry) electrolyte samples, as has been explored preliminarily in prior work.[16] The DSC T_g captured changes in the free volume associated with the α transition (several monomer segments),

whereas the faster timescale of NMR spectroscopy measurements likely allowed smaller-scale dynamics related to polymer architecture to be accessed.[39-41] Notably, the DSC-based interfacial width and $T_{mobility}$ have not been used extensively in the prior literature to analyze polymer dynamics and ion transport and can provide valuable insight into these properties, as described below.

To assess the validity of the framework, NMR spectroscopy and alternating current (AC) impedance spectroscopy were used. NMR spectroscopy was performed to measure the fractions of mobile and immobile polymer, and these fractions were compared to those obtained from the model. Predictions on the basis of the DSC interfacial width and $T_{mobility}$ as input parameters exhibited nearly quantitative agreement with NMR spectroscopy results, suggesting that polymer architecture, segmental mixing, chain stretching, and confinement all must be considered to understand local BP electrolyte dynamics adequately. Next, the modeled local Li^+ and anion diffusivities using the same input parameters (DSC interfacial width and $T_{mobility}$) were spatially averaged across a domain; these predicted diffusivities quantitatively matched ^{7}Li and ^{19}F NMR diffusometry measurements on BP electrolyte samples. In other words, ion diffusivities in these nanostructured systems were captured accurately using knowledge of only the bulk ion diffusivity (*i.e.*, those in POEM HP electrolytes) measurements, bulk $T_{mobility}$ measurements, and interfacial effects. Finally, the modeled local ionic conductivities were spatially summed and compared with BP electrolyte ionic conductivities measured *via* AC impedance spectroscopy. The predicted ionic conductivities overestimated the measurements, likely because ion dissociation[42] and non-random nanostructural orientation[12, 43, 44] effects were not included in the framework. Nevertheless, the qualitative ionic conductivity trends were captured, suggesting that this model can be a powerful tool in the assessment of local ion transport across a mesophase. Altogether, the approach

described herein offers a route toward the elucidation of intra-domain polymer and ion dynamics in BP systems.

MATERIALS AND METHODS

Materials. All materials were stored in a moisture-free, argon-filled glove box after purification. PS (number-average molecular weight [M_n] = 21.1 kg mol^{-1}, dispersity [$Đ$] = 1.18), POEM (M_n = 24.1 kg mol^{-1}, $Đ$ = 1.08, on average 9 EO units per side chain of each repeat unit), and PS-*b*-POEM (M_n = 41.9 kg mol^{-1}, $Đ$ = 1.25, volume fraction of POEM = 0.459) were synthesized and purified as described in prior literature.[14, 16] Li trifluoromethanesulfonate (Li triflate, 99.995%, Sigma-Aldrich) and Li perchlorate (99+%, Acros Organics) were dried under dynamic vacuum at 150 °C for 48 h. Anhydrous tetrahydrofuran (THF, >99%, Optima, not stabilized, Fisher-Scientific) was obtained from a Pure Process Technology, LLC solvent system, in which THF from an argon-pressurized keg was passed through two packed alumina columns.

Electrolyte fabrication. The polymers (PS-*b*-POEM and POEM) and salts (Li triflate and Li perchlorate) were separately dissolved in anhydrous THF at ~20 wt% and stirred for at least 3 h at room temperature (~25 °C), all in an argon-filled glove box. The appropriate masses of polymer and salt stock solutions were mixed to achieve the desired salt concentrations ranging from neat polymer to [Li^+]/[EO] = 0.2 ([EO]:[Li^+] = 5:1, in which [EO] and [Li^+] are the molar concentrations of EO units and Li^+, respectively), and these solutions were stirred for at least 3 h at room temperature (~25 °C). Then, the solutions were sealed in drying chambers and dried under dynamic vacuum for ~16 h at ~25 °C and then ~10 h at 120 °C. The dried electrolytes were stored in an argon-filled glove box prior to characterization.

Small-angle X-ray scattering (SAXS). All SAXS measurements were conducted on a Xenocs Xeuss 2.0 instrument with a sealed-tube X-ray source (Cu Kα, λ = 1.54 Å, 2.0 kW) and Dectris Pilatus 300k 2D detector. Samples were sealed between two Kapton films in an argon-filled glove box and characterized by SAXS under vacuum with a 2000-mm sample-to-detector distance. Under vacuum, samples were annealed at 150 °C for 2 h, cooled to 120 °C and annealed at that temperature for 4 h, and cooled further to 30 °C and held at that temperature for 4 h using a Linkam HFSX350-CAP stage. SAXS profiles were acquired at each temperature after holding for the specified times. Minimal variations were found in the data across all temperatures, and the data reported herein are averages across all measurement temperatures. In **Figure S1**, all 2D scattering data at 30 °C were azimuthally integrated, resulting in plots of scattered intensity versus scattering vector, q. The morphologies were inferred from the ratio of the location of observed scattering peaks (qs) to the location of the primary peak (q^*),[45] as shown in **Figure S1**. The domain spacings (L_{total}s, see **Figure S2**) of the electrolytes were estimated from the primary scattering peak using Eq 1.

$$L_{total} = \frac{2\pi}{q^*} \quad (1)$$

The volume fractions of the conducting domains ($f_{conducting}$s) and interfaces ($f_{int,scattering}$s) in the lamellar samples were calculated from the areas under the Bragg peaks in the SAXS data using Eq 2. The derivation of this equation is described in the literature.[7, 46, 47]

$$\frac{A_{n_x}}{A_{n_y}} = \frac{n_x^{-4}\sin^2\left(n_x\pi f_{conducting}\right)e^{-\frac{1}{2}\pi f_{int,scattering}^2 n_x^2}}{n_y^{-4}\sin^2\left(n_y\pi f_{conducting}\right)e^{-\frac{1}{2}\pi f_{int,scattering}^2 n_y^2}} \quad (2)$$

In Eq 2, A_{nx} and A_{ny} are the areas under Bragg peaks n_x and n_y. The values of n_x and n_y can be 1, 2, 3, etc. corresponding to the q/q^* values for a lamellar morphology. In this work, two Bragg peak ratios, A_1/A_2 and A_1/A_3, were used to solve Eq 2 for the two unknown parameters, $f_{conducting}$ and $f_{int,scattering}$. The mass densities of the conducting domain ($\rho_{conducting}$) calculated on the basis of the $f_{conducting}$s are shown in **Table S1**. The thicknesses of the PS and ion-doped POEM lamellae (L_{PS} and $L_{conducting}$, respectively) were calculated using Eqs 3 and 4, respectively.

$$L_{PS} = \left(1 - f_{conducting}\right)L_{total} \quad (3)$$

$$L_{conducting} = f_{conducting}L_{total} \quad (4)$$

The interfacial thicknesses ($L_{int,scattering}$s) and roughnesses ($L_{rough,scattering}$s) were calculated from Eq 5. For values obtained from SAXS data, $f_{int} = f_{int,scattering}$ calculated from Eq 2.

$$f_{int} = \frac{2L_{int}}{L_{total}} = \frac{2L_{rough}\sqrt{2\pi}}{L_{total}} \quad (5)$$

Both the L_{total}s (**Figure S2**) and $f_{int,scattering}$ (detailed in Results and Discussion sections) were in good agreement with values obtained from X-ray reflectometry (XRR) measurements.[14] The $f_{conducting}$ and f_{int} were used to calculate the local volume fractions of the conducting and PS components [$v_{conducting}(z)$ and $v_{PS}(z)$, respectively, with z as the distance from the center of the

conducting domain normalized by L_{total}], which followed an error function model (Eq 6).[48] The profiles for v_{POEM} and v_{ions} were deconvoluted from the $v_{conducting}$ profile by a method described in the literature.[14]

$$v_{conducting}(z) = 0.5 + 0.5\,\mathrm{erf}\left(\frac{\sqrt{\pi}}{f_{int}}\left(2z + f_{conducting}\right)\right) \quad (6)$$

Standard deviations were calculated by averaging the data at 150, 120, and 30 °C because the L_{total}s, $f_{int,scattering}$s, and $f_{conducting}$s across these temperatures had similar values and did not show systematic changes with temperature. Less than 1.5% uncertainty was calculated for all L_{total}s, and less than 5% uncertainty was obtained for all $f_{int,scattering}$s and $f_{conducting}$s.

Differential scanning calorimetry (DSC). DSC samples were prepared, and measurements were conducted as described elsewhere.[14] Three heating/cooling cycles were performed between -80 and 150 °C at 5 °C min^{-1}, and the second and third traces were compared to verify reproducibility. The T_g values were determined from the midpoints of the inflections in the heating traces. The changes in heat capacity (ΔC_Ps, **Table S2**) at the T_gs were determined by the differences in the baseline C_P values below and above the T_gs in the heating traces for each sample. The reported data were averaged from the second and third heating traces. BP ΔC_P values ($\Delta C_{P,i,BP}$, with i denoting either PS or ion-doped POEM) were found to deviate from the HP ΔC_P values ($\Delta C_{P,i,HP}$), and Morèse-Séguéla et al. proposed that these deviations are indicative of a fraction of the BP domain that is in the interfacial region.[49] This interfacial volume fraction ($f_{int,DSC,i}$) at $T_{g,i}$ was estimated from Eq 7, in which the f_is were obtained from analysis of SAXS data.[49]

$$f_{int,\,DSC,i} = 2f_i\left(1 - \frac{\Delta C_{P,i,BP}}{\Delta C_{P,i,HP}}\right) \quad (7)$$

^{1}H, ^{7}Li, and ^{19}F nuclear magnetic resonance (NMR) spectroscopy and pulsed-gradient stimulated echo (PGSTE) diffusometry. The PS-*b*-POEM samples were packed into the bottom of a 5-mm NMR spectroscopy sample tube outside of a glove box. Then, the packed samples were dried in a hot sand bath at 120 °C under dynamic vacuum for 48 h to remove any moisture. After drying, the samples were flame sealed under vacuum, wrapped in aluminum foil, and stored inside a refrigerator prior to characterization. The POEM HP samples were viscous fluids that adhered to the walls of the sample tube. Thus, these samples were first packed into a 3 × 2 × 10 mm (outer diameter × inner diameter × length) glass tube, then this tube was inserted into a 5-mm sample tube of the same dimensions used for the other samples. The NMR spectra and diffusion data were obtained on a Bruker Avance III 400 MHz/9.4 T wide-bore spectrometer equipped with a single-axis Diff50 diffusion gradient probe (Bruker Diff50), paired with either a 5-mm ^{7}Li/^{31}P radiofrequency (R.F.) insert for ^{7}Li measurements, or a 5-mm ^{1}H R.F. insert for ^{1}H and ^{19}F measurements. ^{35}Cl spectra were not obtained for the samples that contained Li perchlorate due to the extremely fast quadrupole relaxation of the ^{35}Cl nuclei. The measurements were run between -40 and 80 °C in increments of 5 °C. The full width at half maximum (*FWHM*) of these signals had uncertainties of 5%, as determined through a sensitivity analysis that is discussed in greater detail in a companion publication.[50] The ^{1}H NMR spectra of the BP samples exhibited a broad and narrow component, and these components were deconvoluted as shown in **Figure S3**. A sensitivity analysis of the fractions of the broad and narrow components was performed by changing the

widths of the integrated regions (see **Figure S3**); broad/narrow component fractions varied the most at -40 °C (~14%), and this variation decreased as the temperature increased.

The diffusion coefficients of the Li^+ and F-containing anions were obtained at various temperatures using a PGSTE program. The Stejskal-Tanner equation (Eq 8) was fit to the measured signal amplitude (I) as a function of the gradient strength (g).[51]

$$I = I_0 \, exp\left(-D\gamma^2 g^2 \delta^2 \left(\Delta - \frac{\delta}{3}\right)\right) \tag{8}$$

In Eq 8, I_0 is the signal amplitude at $g = 0$, γ is the gyromagnetic ratio, δ is the effective gradient pulse duration, Δ is the diffusion time between gradient pulses, and D is the self-diffusion coefficient. The measurements used a 90° pulse time of 5.5 µs for ^{19}F and 6.25 µs for ^{7}Li, repetition time of 4 s, gradient pulse length of δ = 3 ms, diffusion time of Δ = 100 ms, and acquisition times of 4 ms. Maximum gradient strengths ranging between 1000 and 2300 G/cm, depending on the temperature of the experiment, were used to achieve ≥ 85% signal attenuation in 16 steps. The error in diffusivity values was determined *via* triplicate experiments, showing uncertainties of 10%. It is noted that diffusion measurements were not run on the [EO]:[Li^+] = 5:1 samples because the slow dynamics (short T_2) in these samples limited the temperature range over which reliable diffusion measurements could be obtained.

Alternating current (AC) impedance spectroscopy. Sample preparation and ionic conductivity measurements were performed as described in previous work.[14] The temperature of the samples during annealing and ionic conductivity measurements was regulated using a Linkam HFS91 CAP stage, and electrochemical impedance was measured using a Princeton Applied

Research PARSTAT 2273 frequency response analyzer, all under vacuum. Impedance measurements were performed between 30 °C and 150 °C at 10 °C increments. After holding at each temperature for 5 and 8 min, a voltage amplitude of 10 mV and AC frequency range of 0.1 Hz – 1 MHz was applied to each sample. The touchdown point of the Nyquist plot was defined as the bulk resistance, R_{bulk}. The ionic conductivity, σ_{ionic}, was calculated as

$$\sigma_{ionic} = \frac{L}{R_{bulk} A_{contact}} \tag{9}$$

In Eq 9, L is the sample thickness (0.5 mm), and $A_{contact}$ (0.32 cm^2) is the contact area between the electrolyte and an electrode. The two calculated σ_{ionic} values at each temperature were averaged, and standard deviations from these averages were less than 2%.

RESULTS AND DISCUSSION

The determination of local dynamics in PS-*b*-POEM electrolytes requires an understanding of how the bulk dynamics of the PS and conducting phases are impacted by nanostructure. Bulk dynamics often are inferred from equivalent HP systems, as these HP samples are assumed to be homogeneous and not subject to interfacial phenomena between different mesophases.[34, 52, 53] The HP specimens in this work were studied using DSC and NMR spectroscopy. From these measurements, thermal and mobility transition temperatures of the bulk conducting and non-conducting phases were identified, and the relationship between these temperatures and the polymer architecture was analyzed. Next, two different types of interfacial widths between the PS and conducting mesophases were measured using SAXS and DSC, and the physical contributors to local mobility across an interface were estimated. Then, a quantitative framework was

developed to systematically investigate how the bulk and interfacial behaviors contributed to local polymer dynamics and ion transport. The local polymer mobility and ion diffusivity predictions from this framework were validated using NMR spectroscopy measurements. Ionic conductivity predictions were compared with AC impedance spectroscopy measurements. To distinguish between the results obtained in this work and the interpretation of these results, the contents of this section have been split into "Results" and "Discussion" subsections, respectively.

Identification of thermal and mobility transition temperatures: Results. DSC was employed to study the thermal behavior in the polymer samples, and ^{1}H, ^{7}Li, and ^{19}F NMR spectroscopy were used to examine the polymer, Li^{+}, and anion dynamics, respectively; all data are compiled in **Section S1**, **Figures S4-S5**, and **Tables S3-S4**. In the NMR spectra, the linewidths decreased (indicative of faster dynamics[54]) with increasing temperature. All samples demonstrated a sharp change in the *FWHM* at a certain transition temperature (example shown in **Figure 1a**). The profiles were empirically fit to Eq. 10[16]

$$FWHM = K \tan^{-1}\left(\frac{T - T_{mobility}}{T_{final} - T_{mobility}}\right) + C \qquad (10)$$

in which K is a scaling constant, and C is a shift value determined by taking the average of the largest and smallest *FWHM* values for each profile.[16] The $T_{mobility}$ and T_{final} values represent the midpoint of the inflection (at which the derivative of *FWHM* versus temperature reached a minimum) and the endpoint of the transition, respectively. For a given sample, the $T_{mobility}$s calculated from ^{1}H, ^{7}Li, and ^{19}F NMR spectroscopy were almost identical and were averaged to obtain the mobility transition temperature ($T_{mobility,avg}$, see **Table S3**). As shown in **Figure 1b** and

Table S3, $T_{mobility,avg}$ was higher than the corresponding T_g obtained from DSC experiments for all samples, but the two quantities followed similar trends with salt chemistry and concentration. It is noted that this concept of $T_{mobility}$ was explored in prior work (as the average of $T_{mobility}$ and T_{final} from Eq 10)[16] by examining only the ^{7}Li NMR spectra in PS-*b*-POEM electrolyte systems, and the $T_{mobility}$ values in that work were defined as ion mobility transition temperatures. Herein, $T_{mobility,avg}$ is defined as a transition temperature for both polymer and ion mobility due to the similarities in inflection point values for the ^{1}H, ^{7}Li, and ^{19}F NMR spectra in **Table S3**; *i.e.*, only the polymer contained H atoms, and only the ions contained Li and F atoms, but the *FWHM* versus temperature data for all ^{1}H, ^{7}Li, and ^{19}F NMR spectra showed similar inflection point temperatures for a given sample.

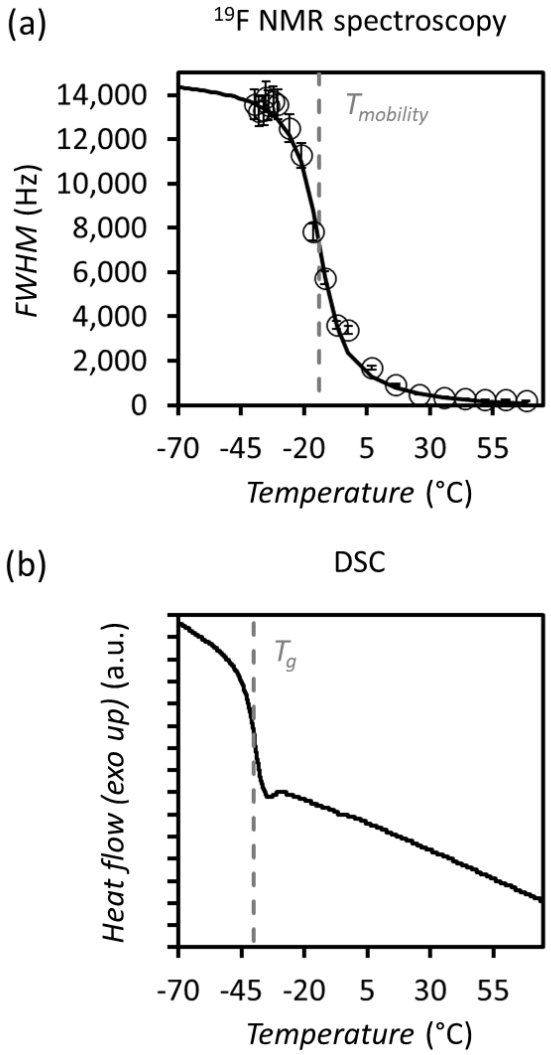

Figure 1. Example of (a) *FWHM* from ^{19}F NMR spectroscopy versus temperature data and (b) heat flow from DSC for Li triflate-doped ([EO]:[Li^+] = 13:1) POEM HP. $T_{mobility}$ and T_g are marked by dashed gray lines. In (a), data points are *FWHM* calculations from ^{19}F NMR spectra, and the solid line represents a fit to Eq 10. In (b), the third heating trace (5 °C min^{-1}, N_2) normalized by total sample mass is shown, and each tick mark on the vertical axis represents a 0.01 W g^{-1} increment. The NMR spectroscopy and DSC data for the remaining samples are compiled in **Figures S4-S5** and **Tables S3-S4** and discussed further in a companion publication (all critical details have been included in this manuscript).[50]

Identification of thermal and mobility transition temperatures: Discussion. The differences between $T_{mobility,avg}$ and T_g likely are related to the size and time scales probed by NMR spectroscopy versus DSC. The DSC T_g is related to the free volume in a polymer system and is indicative of larger-scale α relaxations. Smaller-scale relaxations (*e.g.*, the mobility gradient along a POEM side chain) are not captured by the T_g but are relevant to ion transport.[55, 56] Literature on polymer electrolytes with non-conducting backbones and ionic side-chains also suggests that the characteristic transition temperature for ion motion is significantly different from the DSC T_g.[57] The frequency scale of a DSC measurement was ~10^{-3} Hz,[41] whereas the NMR linewidths for the samples in this study at 30-70 °C were on the order of 10^3-10^4 Hz (**Figure S5**), which gives the approximate frequency of the NMR measurement (inverse of the free induction decay time). In this same temperature range, the characteristic frequency of the Nyquist plot touchdown in the AC impedance spectroscopy measurements was on the order of 10^1-10^3 Hz, which is similar to the frequency range of the NMR spectroscopy measurements. Thus, $T_{mobility,avg}$ might be more appropriate than T_g for predicting ion transport. In **Figure S3**, the difference between $T_{mobility,avg}$ and T_g for the PS HP was 7.5 °C, but the differences between $T_{mobility,avg}$ and T_g for the neat and ion-doped POEM HP samples were larger (~20-30 °C), which might be the result of the polymer architectures. The long POEM side chains, relative to the size of the aromatic PS pendant group, might have a larger mobility gradient, leading to greater discrepancies between larger- and smaller-scale dynamics. For instance, the T_g value for the POEM HP samples might be more representative of the free ends of the side chains, which likely have the greatest free volume relative to the rest of the POEM molecule, whereas $T_{mobility,avg}$ might be more representative of the average mobility along the POEM side chain.

Identification of interfacial widths using SAXS and DSC: Results. Figure 2 shows the volume fractions of the interfaces, f_{int}, between the PS and conducting domains, obtained from analysis of X-ray scattering ($f_{int,scattering}$) and DSC ($f_{int,DSC}$) data. In **Figure 2a**, the $f_{int,scattering}$s from the current study were compared to f_{int}s calculated from XRR data from a prior study that used the same PS-*b*-POEM BP (**Figure 2a**).[14] The SAXS- and XRR-based f_{int}s were in good agreement. In **Figures 2b** and **2c**, $f_{int,DSC,conducting}$ and $f_{int,DSC,PS}$ values, respectively, were calculated according to Eq 7. The $f_{int,DSC,conducting}$ values were smaller in magnitude than the $f_{int,DSC,PS}$ values, and the $f_{int,DSC}$ values were larger than the $f_{int,scattering}$ values for all samples.

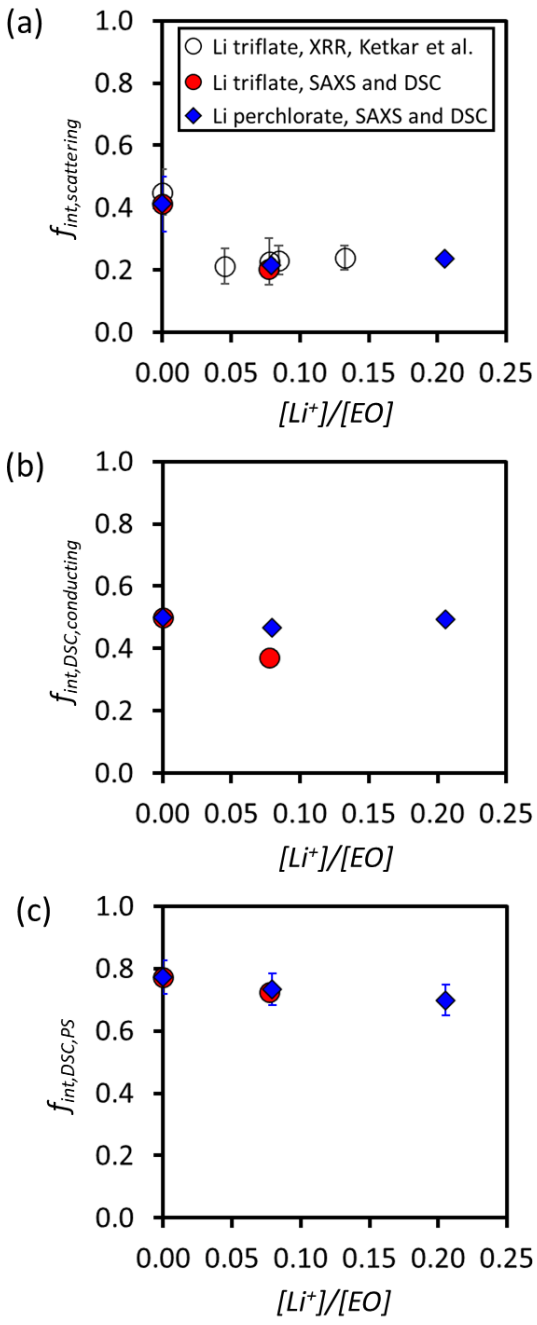

Figure 2. Volume fraction of the interfacial region, f_{int}, in lamellar PS-*b*-POEM electrolytes as determined from (a) X-ray scattering data, (b) DSC measurements of $\Delta C_{P,conducting}$, and (c) DSC measurements of $\Delta C_{P,PS}$. Error bars for the SAXS data in (a) represent one standard deviation from the $f_{int,scattering}$ values obtained from SAXS measurements at 30 °C, 120 °C, and 150 °C. Error bars

for the XRR data in (a) are propagated uncertainties from the roughness parameters obtained from XRR fits. Error bars in (b) and (c) are propagated uncertainties of ΔC_P values calculated from DSC and $f_{conducting}$ values calculated from SAXS. The XRR data in (a) were adapted with permission from reference 14. Copyright (2021) American Chemical Society.

Identification of interfacial widths using SAXS and DSC: Discussion. The results in **Figure 2** can be understood by considering the physical phenomena that were probed by SAXS and DSC. In **Figure 2a**, the hard X-rays used in both the SAXS and XRR measurements were sensitive to the scattering length density, which captures segmental mixing effects in BP systems. The SAXS measurements were run on bulk electrolyte samples that contained multiple randomly oriented nanostructured grains. On the other hand, XRR measurements were conducted on thin film samples that contained lamellae that were all oriented parallel to the substrate, as verified by atomic force microscopy.[14] The agreement between SAXS and XRR results in **Figure 2a** suggests X-ray-based $f_{int,scattering}$ is minimally sensitive to grain size and orientation. In contrast to hard X-ray scattering, DSC measurements likely are sensitive to a combination of segmental mixing, chain stretching, and confinement that together perturb the thermal behavior (*i.e.*, $f_{int,scattering}$ may be related to the compositional gradient within a domain, and $f_{int,DSC}$ may be more related to the mobility gradient in that domain). Thus, the larger values of $f_{int,DSC,conducting}$ and $f_{int,DSC,PS}$ relative to $f_{int,scattering}$ suggest that chain stretching, confinement, etc. extended beyond the length scale of segmental mixing near the interface. Specifically, the decrease in $L_{int,scattering}$ (**Figure S6a**) with ion concentration versus the increase in $L_{int,DSC}$ (**Figures S6b** and **S6c**) implied that the decrease in segmental mixing was accompanied by an increase in chain stretching; slight increases in $L_{int,scattering}$ at higher salt loadings (**Figure S6a**) likely were the result of the buckling of lamellae

prior to a morphological transition.[17] The larger magnitude of $f_{int,DSC,PS}$ relative to $f_{int,DSC,conducting}$ was likely the result of greater interfacial mixing at higher temperatures corresponding to $T_{g,PS}$ (~100 °C, relative to $T_{g,conducting}$, which ranged from -60 °C to 14 °C). The temperature dependence of $f_{int,DSC}$ is discussed further in the Supporting Information (**Section S2** and **Figures S7-9**).[14, 17, 58-64]

Development of a quantitative framework to describe local polymer dynamics: Results. To probe the combined impact of polymer architecture, segmental mixing, chain stretching, and confinement on polymer dynamics, a quantitative framework was developed to predict local polymer mobilities. A schematic of the approach is shown in **Figure 3** using data from a Li triflate-doped BP sample at [EO]:[Li^+] = 13:1. In **Figure 3a**, the local v_{PS}, v_{POEM}, and v_{ions} profiles were obtained from Eq 6 (using $f_{int,scattering}$ in this example). Local transition temperatures [$T_{transition}(z)$, referring to $T_g(z)$ or $T_{mobility,avg}(z)$] of the S and OEM segments were estimated using the Fox equation and the data in **Figure 3a**, bulk transition temperature measurements of the PS and Li triflate-doped POEM HPs ($T_{transition,bulk,PS}$ and $T_{transition,bulk,conducting}$, respectively, which refer to either the bulk T_g [measured *via* DSC] or $T_{mobility,avg}$ [measured *via* NMR spectroscopy] values), and self-concentration effects.[7] It is noted that the Fox equation is most appropriate for cases in which the components have minimal specific interactions.[65] This assumption was applied to model a mixture between the PS and conducting phases, as PS is known to not have attractive interactions with POEM or the salts used in this study.[18, 66] On the other hand, POEM and lithium salts are known to have significant specific interactions with each other,[55] and thus, bulk transition temperatures were measured for mixtures of POEM HP and lithium salts, instead of predicted from the Fox equation. These measured transition temperatures were assumed

to be representative of the conducting-phase bulk transition temperatures in the equivalent BP systems because prior studies on Li triflate- and Li perchlorate-containing PS-*b*-POEM have demonstrated that the ion distributions were proportional to the POEM distributions.[17, 18] For BP systems in which these simplifications are not valid, a more rigorous model is recommended; some models that account for specific intermolecular interactions are discussed in a review by Schneider.[65]

Although compositional distributions of the PS, POEM, and ions as a function of z have been determined through SAXS in Eq 6, these profiles do not account for self-concentration effects that arise as a result of chain connectivity.[7, 37] For example, the center of an interface between the PS and conducting phases may contain ~50 vol% PS on average, but the PS might not be mixed homogeneously with the POEM and ions located at the same z. Thus, these self-concentration effects were modeled in the present study using the framework proposed by Lodge and McLeisch.[37] Self-concentration can be described as a function of the repeat unit molar mass (M_0), average length of a backbone bond (l), number of backbone bonds per repeat unit (k), Avogadro's number (N_{Av}), mass density (ρ), and the statistical segment length (b).[37] In this work, $M_{0,PS}$ = 104 g mol^{-1}, and $M_{0,POEM}$ = 500 g mol^{-1}, which is the number-average molar mass of POEM monomer segments determined from solution-state ^{1} NMR spectroscopy. The value of l was estimated as 0.153 nm because both PS and POEM have sp^3-hybridized carbon atoms in the backbone,[67] and $k_{PS} = k_{POEM} = 2$. For the PS phase, ρ_{PS} = 1.05 g cm^{-3} and b_{PS} = 0.68 nm were set as constant values for all samples. These values were simplified as constants because ρ_{PS} varies only by ~5% over the temperature range considered in this study.[68] For systems with larger ρ or b variations, it is recommended to include the temperature dependences to obtain more rigorous calculations of self-concentration. For the conducting phase, $\rho_{conducting}$s were calculated for each

sample separately in **Table S1**, and the $b_{conducting}$s were estimated through strong-segregation-theory calculations (**Figure S5d-f**).[17] Although self-concentration analyses most often have been applied to miscible blends, it was assumed that this framework is applicable to BP systems because self-concentration primarily is attributed to chain connectivity rather than thermodynamic interactions between unlike segments.[7, 37]

The self-concentration fractions of the conducting phases were closer to 0, and those in the PS phases were closer to 1 in all samples. These values followed the expectations for self-concentration behavior of rubbery and glassy polymers, respectively.[7] In practice, the apparent self-concentration also can decrease relative to the theoretical self-concentration if the neighboring phase exhibits low fragility,[69] but these effects were not considered in this work because both the PS and conducting phases were expected to have high fragility. Generally, many polymers exhibit high fragility, and the fragility is expected to increase as chain relaxation is impeded, such as in high-segregation-strength BPs (due to high interfacial chain stretching) and in ion-doped polymer electrolytes (due to ion-polymer interactions).[70-72] Moreover, the scaling of self-concentration with b could be modeled more rigorously (*e.g.*, with a prefactor, decaying function, or some function of z to account for variable chain statistics versus distance from the interface). These complexities were not incorporated into the current model because prior literature has demonstrated agreement between experiments and predictions using the simplified scaling with b.[37]

Altogether, $T_{transition}(z)$s were estimated using Eq 11:

$$T_{transition,i}(z) = \frac{1}{\frac{\frac{M_{0,i}\left(1-v_i(z)\right)}{k_i l_i \rho_i N_{Av} b_i^2}+v_i(z)}{T_{transition,bulk,i}} + \frac{1-\frac{M_{0,i}\left(1-v_i(z)\right)}{k_i l_i \rho_i N_{Av} b_i^2}-v_i(z)}{T_{transition,bulk,j}}} \quad (11)$$

Eq. 11 facilitated the calculation of $T_{transition,conducting}(z)$ and $T_{transition,PS}(z)$ profiles separately; when *i* referred to POEM, *j* referred to PS, and when *i* referred to PS, *j* referred to POEM. An example of a $T_{transition,conducting}(z)$ profile is shown in **Figure 3b**.[7, 37] From this profile, the fraction of mobile and immobile polymer could be calculated. If this sample were probed at 30 °C, for example, monomer segments with a $T_{transition}(z)$ above 30 °C would be considered immobile (**Figure 3c**), whereas segments with a $T_{transition}(z)$ below 30 °C would be considered mobile (**Figure 3d**).

The use of $f_{int,scattering}$ versus $f_{int,DSC}$ and $T_{g,conducting}$ versus $T_{mobility,avg,conducting}$ as model input parameters was compared to determine which set of parameters provided a more accurate description of polymer dynamics. It is noted that $f_{int,scattering}$ was held constant across all temperatures in the model, whereas $f_{int,DSC}$ varied with temperature, as defined by strong-segregation-theory calculations[17] and the temperature dependence of the effective interaction parameter, χ_{eff} (**Section S2**).

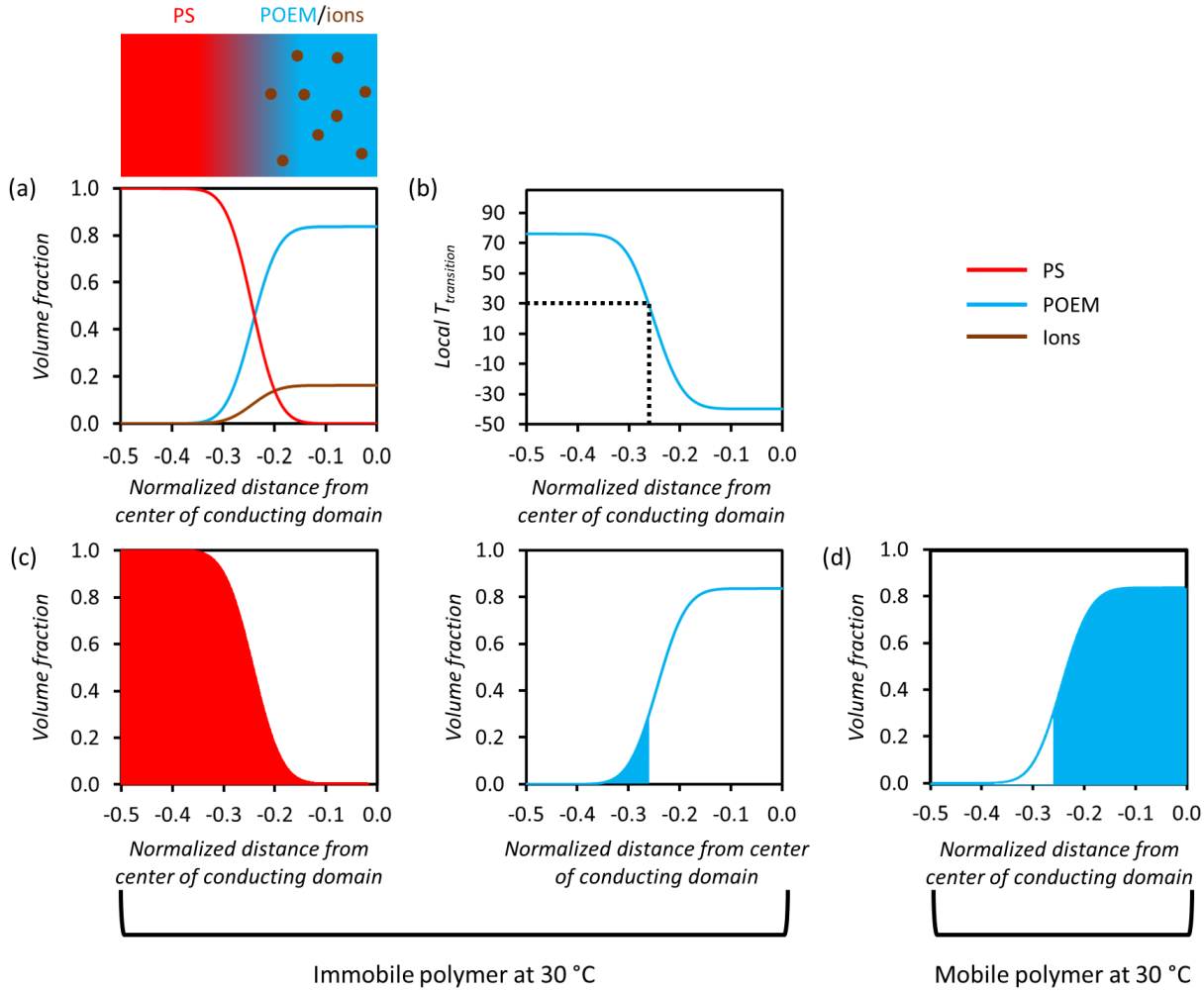

Figure 3. Example schematic for the modeling of $T_{transition}(z)$ in Li triflate-doped ([EO]:[Li^+] = 13:1) PS-*b*-POEM. (a) Distributions of S, OEM, and ions for half of a domain, in which the left side of the plot represents the center of the PS domain, and the right side represents the center of the conducting domain (also depicted in the cartoon above). The data in this example are obtained from SAXS measurements. (b) $T_{transition}(z)$s of OEM segments are estimated from the compositional data in (a) as well as self-concentration behavior. As an example, the position in the domain at which the $T_{transition}(z)$ is equal to 30 °C is depicted. (c) The shaded regions of the PS and POEM domains are those for which the $T_{transition}(z)$ is greater than the hypothetical measurement

temperature of 30 °C, and thus, those regions are considered immobile. (d) The shaded region of the POEM domain is that for which the $T_{transition}(z)$ is less than 30 °C, and thus, this region is considered mobile. This model has been applied to all samples investigated in this work.

The predicted mobile/immobile polymer fractions were validated using ^{1}H NMR spectroscopy measurements on the same solid (dry) electrolyte samples (**Figure 4a**). The ^{1}H NMR signals contained narrow and broad components, which represented mobile and immobile protons (*i.e.*, protons that tumbled faster and slower than the ~ 10 kHz frequency of the ^{1}H-^{1}H dipole-dipole couplings in the samples), respectively. The fractions of areas under the narrow and broad components were deconvoluted in the manner shown in **Figure S3** (and Figure S6 of a companion publication).[50] A combination of $f_{int,DSC}$ and $T_{mobility,avg}$ (of both the conducting and PS domains) as model input parameters resulted in nearly quantitative matches between the predicted fractions of mobile/immobile protons and the calculated fractions of mobile/immobile protons from the ^{1}H NMR spectroscopy results (**Figures 4b-e**).

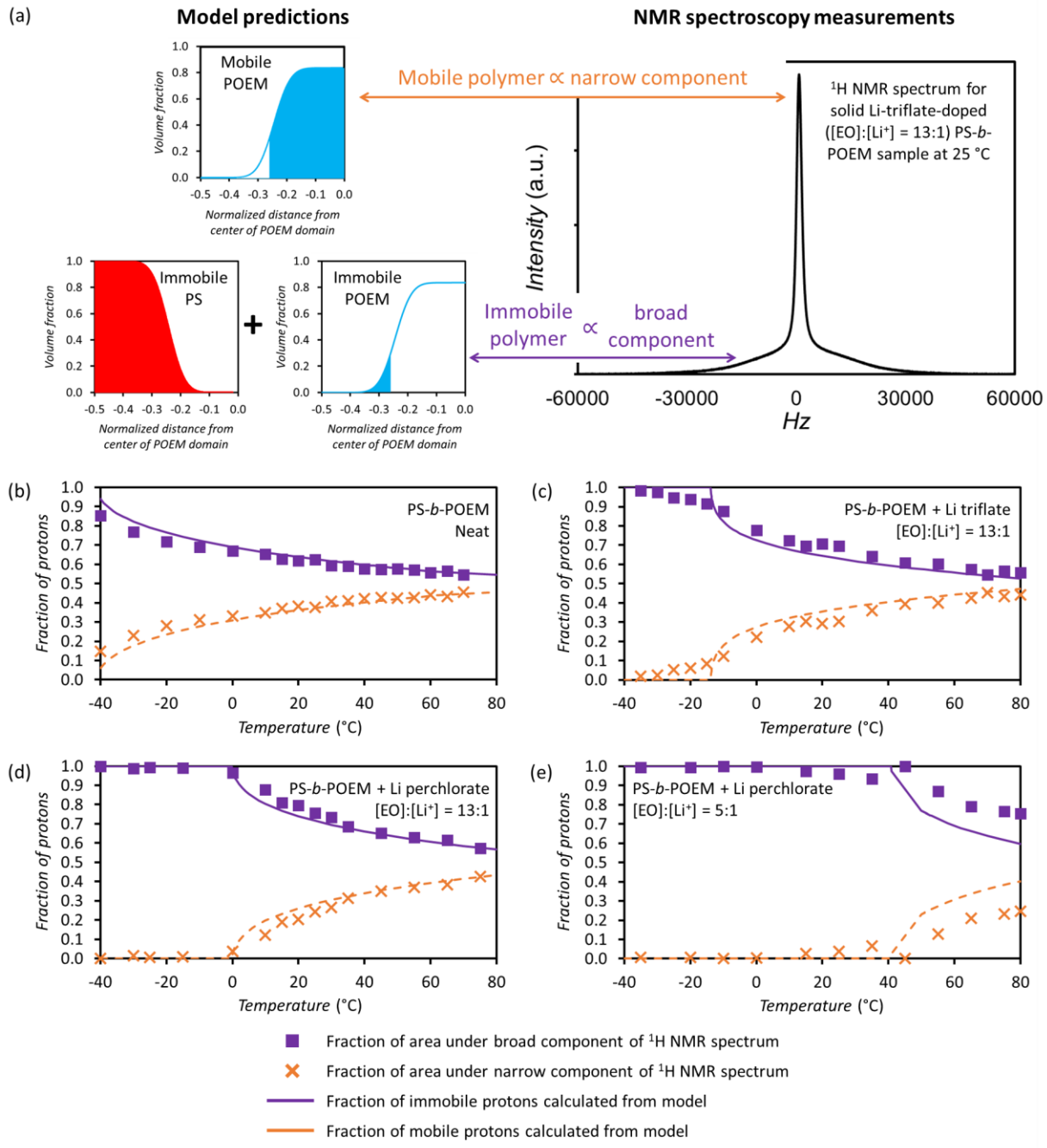

Figure 4. (a) Schematic illustration to demonstrate the comparison of predicted mobile and immobile polymer fractions to the fractions of broad and narrow components in ^{1}H NMR spectra. (b-e) Comparison of ^{1}H NMR spectroscopy results (data points) and modeling (lines) using $f_{int,DSC}$, $T_{mobility,avg,conducting}$ and $T_{mobility,PS}$ as input parameters for (b) neat PS-*b*-POEM, (c) Li triflate-doped

PS-*b*-POEM at [EO]:[Li^+] = 13:1, (d) Li perchlorate-doped PS-*b*-POEM at [EO]:[Li^+] = 13:1, and (e) Li perchlorate-doped PS-*b*-POEM at [EO]:[Li^+] = 5:1.

Development of a quantitative framework to describe local polymer dynamics: Discussion. The agreement between the ^{1}H NMR spectroscopy data and model predictions in **Figures 4b-e** suggested that the polymer architecture, segmental mixing, chain stretching, and confinement all significantly contributed to the polymer dynamics. The results in **Figure 4** were compared to those in which $f_{int,scattering}$ and T_g were used as the model input parameters (**Figures S10-S13**). Negligible differences were noted between the predicted values that used $f_{int,scattering}$ versus $f_{int,DSC}$ in the neat BP (**Figure S10**), but substantial deviations were found in the salt-doped samples (**Figures S11-S13**). Likely, the neat BP had a low enough segregation strength, such that the effects of compositional mixing were more significant than of chain stretching (*i.e.*, the dynamical gradient was dominated by compositional mixing). In the higher-segregation-strength salt-doped samples, however, the decrease in compositional mixing ($f_{int,scattering}$) likely occurred concomitantly with an increase in chain stretching, which could contribute to a larger $f_{int,DSC}$. The significantly lower values of $f_{int,scattering}$ versus $f_{int,DSC}$ resulted in an overestimation of the amount of mobile polymer in the salt-doped specimens and suggested that segmental mixing alone does not explain polymer dynamics, especially at the high segregation strengths.

Similarly, the use of T_g instead of $T_{mobility,avg}$ resulted in an overestimation of the fraction of mobile polymer, especially at low temperatures. This outcome is consistent with results from prior literature, in which the average EO relaxation rate in POEM was significantly below that in poly(ethylene oxide) (PEO, the relaxation rate of which can be understood as the intrinsic EO relaxation rate) at low values of $T - T_g$, but was closer to the predictions at higher temperatures

closer to $T_{g,PS}$.[55, 56] The $T_{g,conducting}$ is associated with the α transition at which the relaxation of multiple monomer segments is achieved, but $T_{g,conducting}$ does not provide information about the local relaxation of the side chains or individual EO groups, which are associated with the β and γ transitions.[39, 40] The use of NMR spectroscopy linewidths (and the associated $T_{mobility,avg,conducting}$) enabled architectural effects to be captured because the high frequency (400 MHz) of the measurements facilitated the probing of additional relaxations associated with the POEM side chains and individual EO units. Although the experimental validation measurements of mobile and immobile polymer in **Figure 4** also were obtained from NMR spectroscopy, using an NMR-spectroscopy-derived input (*i.e.*, $T_{mobility,avg}$) in the model alone does not necessarily result in quantitative matches between the model and experiments (*e.g.*, see **Figure S12c** versus **S12d**). The input $T_{mobility,avg}$ values only impacted the location of the inflection points but not the shape of the curve (*e.g.*, see **Figure S12a** versus **S12c**). Thus, the results in **Figure 4** more strongly validate the use of $f_{int,DSC}$ to provide an accurate description of the dynamic gradient across an interface. It is possible to draw similar comparisons using different techniques (*e.g.*, dynamic mechanical analysis to explore the effects of measurement frequency on $T_{mobility}$,[41] neutron spin echo spectroscopy to assess material relaxation timescales[73]), but in many cases, the characterization of ion dynamics becomes more challenging.

It is noted that there was a slight discrepancy between the model and NMR spectroscopy data in **Figure 4b-c** at low temperatures, and there are a few factors that may have contributed to this discrepancy. In the NMR spectroscopy experiments, the overlap of the broad and narrow components at low temperatures resulted in greater uncertainty during the deconvolution of the areas of those components, as the calculation used to determine the ratio assumed the narrow component to lie on top of the broad component with minimal overlap (**Figure S3**). In the model,

any segments with $T_{transition}(z)$ above the hypothetical measurement temperature were considered to be completely immobile even though there may be a slight onset of polymer mobility at temperatures slightly below $T_{transition}(z)$. At the moment, it is unclear why there was a discrepancy between the predictions and measurements at high temperatures in **Figure 4e**, but it is noted that the combination of $f_{int,DSC}$ and $T_{mobility,avg}$ as model input parameters still provided the closest match to the ^{1}H NMR spectroscopy data relative to other combinations of input parameters (**Figure S13**). Regardless, the overall close agreement between NMR spectroscopy data and predicted values suggested these sources of error are minimal and that NMR spectroscopy can be used reliably to gain insight into local dynamics. For example, prior frameworks, such as that proposed by Sax and Ottino,[74] suggest that the bulk average transport rate is proportional to the compositional volume fraction of the conducting phase, which changes minimally with temperature. The accuracy of such frameworks can be improved by correcting for the temperature-dependent portion of the conducting phase that is mobile versus immobile; this concept is explored further in a companion publication.[50] It is emphasized that the quantitative matches between the model and ^{1}H NMR spectroscopy data in this work were obtained without the use of any floating parameters in the model (*i.e.*, the predicted values were determined *a priori*).

Prediction of local ion diffusivities and ionic conductivities: Results. The model depicted in **Figure 3** was extended to predict ionic conductivities in BP electrolytes using knowledge of equivalent HP electrolytes (representative of the bulk conducting material) and the dynamical gradient induced by the nanostructure (*i.e.*, obtained from Eq 11, in which $T_{mobility,avg}$ and $f_{int,DSC}$ were the input parameters). First, local diffusivities were calculated *via* the Vogel-Fulcher-Tamman (VFT) equation (Eq 12).[72]

$$D_i(z) = f_{morphology} D_{0,HP,i} \exp\left(-\frac{E_{a.HP,i}}{R\left(T - T_{0,i}(z)\right)}\right) \quad (12)$$

In Eq 12, $f_{morphology}$ is the morphology factor, $D_{0,i}$ is the pre-exponential factor, $E_{a,i}$ is the activation energy of ion motion, R is the gas constant, and $T_{0,i}(z)$ is the local Vogel temperature (i denoted either Li^+ or the anion). The $f_{morphology}$ parameter accounts for the fraction of nanostructural orientations that contribute to ionic conductivity at a length scale larger than the grain size in one dimension. For samples that form lamellae, $f_{morphology} = 2/3$.[74] The $D_{0,i}$ and $E_{a,i}$ parameters in Eq 12 were set equal to the equivalent parameters in the corresponding POEM HP system measured by NMR diffusometry (**Section S3** and **Figure S14**); it was assumed the $D_{0,i}$ and $E_{a,i}$ parameters for the Li^+ and anion diffusivity were minimally impacted by the BP nanostructure. In this work, $T_{0,i}(z)$ was set equal to $T_{transition,conducting}(z)$ - 50 K,[75] in which $T_{transition,conducting}(z)$ was calculated from Eq 11. Local molar ionic conductivities were predicted by using the Nernst-Einstein equation (Eq 13).

$$\sigma_{ionic,molar}(z) = \frac{F^2}{RT}\left(D_{Li^+}(z) + D_{anion^-}(z)\right) \quad (13)$$

In Eq 13, F is Faraday's constant, T is the measurement temperature, and $D_{Li+}(z)$ and $D_{anion-}(z)$ can be determined from Eq 12.

An example of the predicted local Li^+ and anion diffusivities for Li triflate-doped ([EO]:[Li^+] = 13:1) PS-*b*-POEM at 30 °C is shown in **Figure 5a**. These diffusivity profiles were overlaid on top of the estimated ion distribution in the same sample, showing that regions with higher ion content also had faster ion diffusion. To check the validity of the modeled $D_i(z)$ from

Eq 12, a weighted average of $D_i(z)$ was taken according to Eq 14 and compared with the measured ion diffusivities of the corresponding BP electrolyte.

$$D_{avg,BP,i} = \frac{\sum_{z=-0.5}^{z=0} D_i(z) * v_{ions}(z)}{\sum_{z=-0.5}^{z=0} v_{ions}(z)} \quad (14)$$

It is noted that although $f_{int,DSC}$ was used in Eq 11-13 to accurately quantify polymer and ion dynamics, $f_{int,scattering}$ was used to obtain the compositional ion distribution [$v_{ions}(z)$] in Eq 14. $D_{avg,BP,Li+}$ and $D_{avg,BP,anion-}$ were calculated for all temperatures at which ion diffusivities were measured, and the predictions agreed well with the measured Li^+ and anion diffusivities (from NMR diffusometry) in **Figure 5b**. Similar agreement was achieved between the modeled and measured Li^+ diffusivity in an equivalent Li perchlorate-doped sample (**Figure S15a**).

An example of the predicted $\sigma_{ionic,molar}(z)$ for Li triflate-doped BP at 30 °C is shown in **Figure 5c**. Bulk ionic conductivities were estimated by taking a weighted sum of the local molar ionic conductivities (from Eq 13), as shown in Eq 15.

$$\sigma_{ionic,total} = 2 \int_{-0.5}^{0} \sigma_{ionic,molar}(z) v_{ions}(z) \frac{\rho_{ions}}{M_{ions}} dz \quad (15)$$

In Eq 15, the mass density of the ions, ρ_{ions} is approximated as the bulk mass density of the lithium salt (1.90 g cm^{-3} for Li triflate and 2.42 g cm^{-3} for Li perchlorate), and M_{ions} is the molar mass of the salt (156.01 g mol^{-1} for Li triflate and 106.39 g mol^{-1} for Li perchlorate). The integral in Eq 15 was calculated across half a domain and then multiplied by 2 to capture the total conductivity in a full domain, as the compositional and dynamical profiles were assumed to be symmetric in a

lamellar domain. It is noted that a weighted average was used in Eq 14 because the measured diffusivity (intensive quantity) represents an average ionic mobility, which does not scale with total ion content. On the other hand, a weighted sum was used in Eq 15 because the measured ionic conductivity (extensive quantity) is proportional to the total number of charged species. The predicted ionic conductivities for the Li triflate-doped BP were overlaid onto the measured ionic conductivities measured by AC impedance spectroscopy for this sample in **Figure 5d**. The predicted conductivities were ~4 times larger than the respective measured ionic conductivities. Ionic conductivity model estimations for the Li perchlorate-doped BP are detailed in **Section S3** and **Figure S15b**.

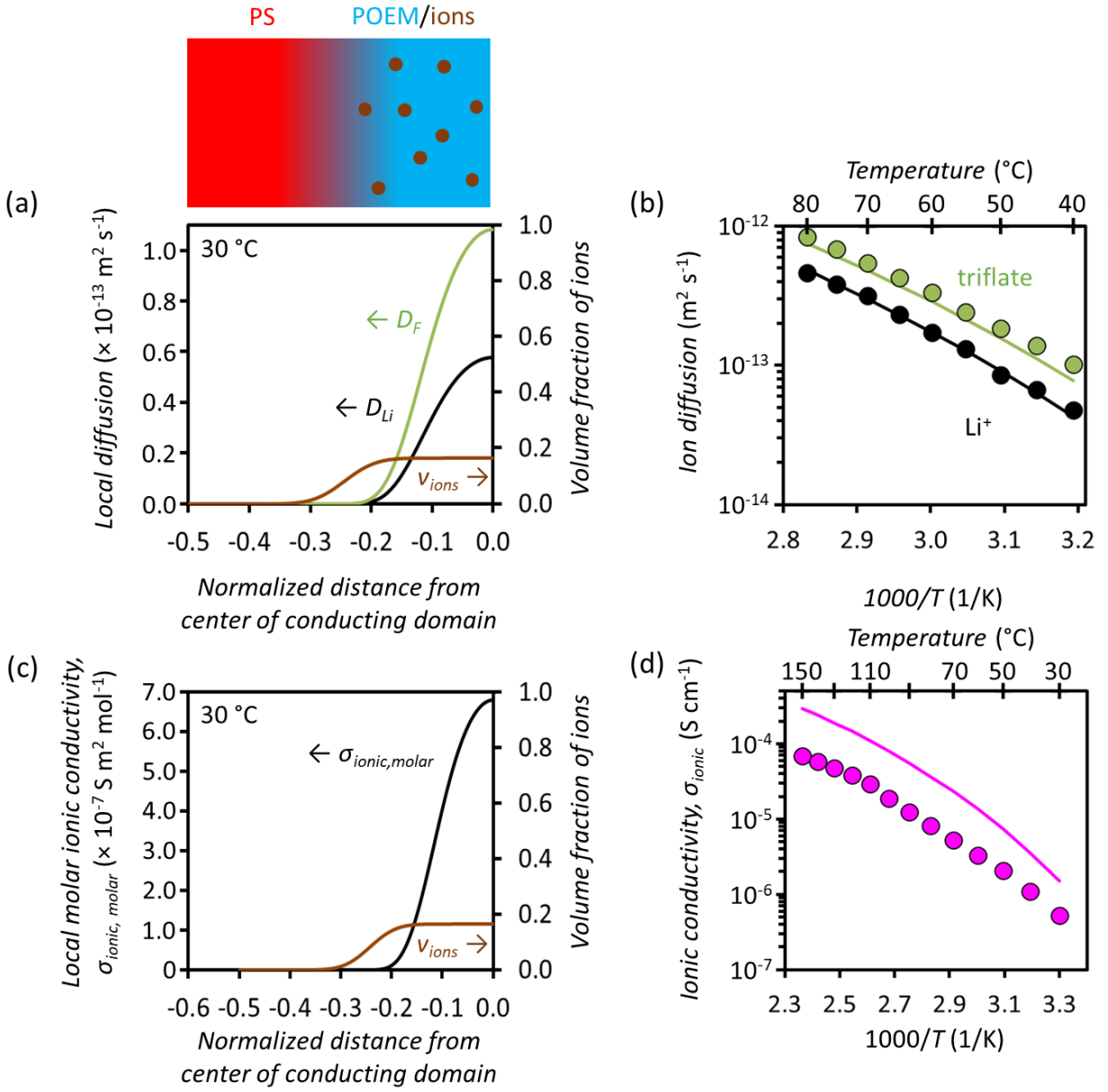

Figure 5. (a) Local Li^+ and anion diffusivities (left-hand axis, calculated from Eq 12) and local volume fraction of ions (right-hand axis, calculated from Eq 6) across half a lamellar domain for Li triflate-doped ([EO]:[Li^+] = 13:1) PS-*b*-POEM at 30 °C. (b) Ion diffusion measurements (data points, obtained *via* NMR diffusometry) and predictions from the weighted averaging of local modeled diffusivity (lines, calculated from Eq 14) versus 1000/*T*. (c) Local molar ionic conductivities (left-hand axis, calculated from Eq 13) and local volume fraction of ions (right-hand

axis, calculated from Eq 6) across half a lamellar domain for Li triflate-doped ([EO]:[Li^+] = 13:1) PS-*b*-POEM at 30 °C. (d) Ionic conductivity measurements (data points, obtained *via* AC impedance spectroscopy) and predictions from the weighted summation of local modeled conductivity (lines, calculated from Eq 15) versus 1000/*T*. Error bars for the data points in (b), most of which are smaller than the depicted data point, are standard deviations from triplicate measurements. Error bars for the data points in (d), most of which are smaller than the depicted data point, are the standard deviation obtained by averaging two ionic conductivity measurements at each temperature.

Prediction of local ion diffusivities and ionic conductivities: Discussion. The Haven ratios (ratios of predicted ionic conductivities to measured ionic conductivities) in **Figure 5d** were larger than those found experimentally for Li TFSI-doped PEO[76] but closer to some Haven ratios for equivalent simulated systems.[77] These Haven ratios, in part, account for the incomplete dissociation of the salts. In nanostructured systems, the non-random morphological orientations near the electrode surface in the ionic conductivity measurements also can impact the Haven ratios, especially for lamellar samples.[12, 34, 43, 44] Ionic conductivity model estimations for the Li perchlorate-doped BP are discussed in **Section S3** and **Figure S15b**.[38, 78-80] Although the predicted ionic conductivities in **Figure 5d** did not quantitatively match the measured ionic conductivities, both datasets qualitatively followed similar trends with respect to temperature. Moreover, the predicted average ion diffusivities quantitatively matched the measured diffusivities, demonstrating that ion mobilities are accurately represented by the approach presented in this work. In contrast, it is shown in **Figure S16** that simple multiplication of the HP diffusivities by $f_{morphology}$ does not lead to agreement with the BP diffusivities, suggesting that the ion diffusivity

differences between the BP and HP samples cannot be explained by morphological orientations, alone. Instead, the interfaces also might impact local ion transport significantly, and the combined effects of morphological orientations and local heterogeneity near the interfaces can be captured through Eq 12. The knowledge of local ion dynamics afforded through this framework can enable regions with lower ion mobilities to be identified and guide the design of electrolyte systems that enhance transport at targeted locations within a domain.

CONCLUSIONS

Herein, a quantitative model for the intra-domain polymer and ion dynamics in PS-*b*-POEM electrolytes was developed using knowledge of bulk dynamics (inferred from homopolymer systems) and interfacial behavior between the conducting and non-conducting mesophases. Local polymer mobility and ion diffusivity predictions from this model were validated through NMR spectroscopy and diffusometry experiments. Comparison of the model predictions to the NMR results suggested that the polymer and ion dynamics were a strong function of the polymer architecture, segmental mixing, chain stretching, and confinement. Using these insights, the model in this study enabled the assessment of local ion transport from the reference point of local mobility transition temperatures. This approach can provide an improvement to the understanding of ion dynamics over the conventional approach of empirically correlating the total ionic conductivity to an average polymer glass transition temperature or relaxation timescale. Especially as low-segregation-strength systems with wide interfaces are beginning to show promise as efficient electrolytes, the model developed in this study can facilitate the assessment of local transport in a conducting domain. Moreover, this framework can be applied to examine the local structure and segmental dynamics in a variety of electrolyte and non-electrolyte systems (*e.g.*,

nanostructured elastomers, thin-film nanotemplates) that span a wide range of polymer/additive chemistries toward the rational design of macromolecular materials.

ASSOCIATED CONTENT

Supporting Information. SAXS profiles; domain spacings from SAXS and XRR measurements; volume fractions and mass densities of the conducting domains in BP electrolytes; ΔC_P results from DSC measurements; determination of areas of broad and narrow components from ^{1}H NMR spectroscopy; DSC traces for HP and BP samples; *FWHM* versus temperature profiles from NMR spectroscopy for HP and BP samples; T_g and $T_{mobility}$ results in HP and BP systems; interfacial thicknesses from SAXS and DSC measurements; strong-segregation-theory analyses of SAXS and DSC data; enthalpic and entropic contributions to χ_{eff}; comparisons of χ_{eff} versus temperature from SAXS and DSC data; comparisons of mobile/immobile polymer fractions ^{1}H NMR spectroscopy measurements and modeled predictions; ion diffusion data for HP electrolytes; predicted ion diffusivities and conductivities for Li perchlorate-doped electrolyte; comparisons of ion diffusivities in BPs and scaled ion diffusivities in HPs

AUTHOR INFORMATION

Corresponding Authors

Louis A. Madsen – Department of Chemistry and Macromolecules Innovation Institute, Virginia Polytechnic Institute and State University, Blacksburg, Virginia 24061, United States; orcid.org/0000-0003-4588-5183; Email: lmadsen@vt.edu

Thomas H. Epps, III – Department of Chemical & Biomolecular Engineering and Department of Materials Science & Engineering, University of Delaware, Newark, Delaware 19716, United States; orcid.org/0000-0002-2513-0966; Email: thepps@udel.edu

Authors

Priyanka M. Ketkar – Department of Chemical & Biomolecular Engineering, University of Delaware, Newark, Delaware 19716, United States; orcid.org/0000-0001-8891-4808

Nicholas F. Pietra – Department of Chemistry and Macromolecules Innovation Institute, Virginia Polytechnic Institute and State University, Blacksburg, Virginia 24061, United States; orcid.org/0000-0003-3250-728X

Andrew G. Korovich – Department of Chemistry and Macromolecules Innovation Institute, Virginia Polytechnic Institute and State University, Blacksburg, Virginia 24061, United States; orcid.org/0000-0003-3736-1523

Author Contributions

The manuscript was written through contributions of all authors. All authors have given approval to the final version of the manuscript.

Notes

The authors declare no competing financial interest.

ACKNOWLEDGMENT

P.M.K. and T.H.E. thank a Department of Energy grant (DOE BES; DE-SC0014458) for financial support during polymer synthesis, sample preparation, and sample characterization. Data analysis was conducted with partial support to T.H.E. under cooperative agreement 70NANB12H239 from NIST, U.S. Department of Commerce. N.F.P., A.G.K., and L.A.M. thank a National Science Foundation grant (DMR Polymers – 1810194) for financial support during the NMR spectroscopy characterization of solid (dry) electrolyte samples. The authors thank Dr. Melody A. Morris for the synthesis of the PS and POEM homopolymers. Certain commercial equipment, instruments, materials, suppliers, or software are identified in this paper to facilitate the understanding and interpretation of data. Such identifications do not imply recommendation or endorsement by DOE, NSF, NIST, or the U.S. Department of Commerce nor do they imply that the materials or equipment identified are necessarily the best available for the purpose.

REFERENCES

1. Young, W.-S.; Kuan, W.-F.; Epps, T. H., III, Block copolymer electrolytes for rechargeable lithium batteries. *Journal of Polymer Science, Part B: Polymer Physics* **2014,** *52* (1), 1-16.
2. Morris, M. A.; An, H.; Lutkenhaus, J. L.; Epps, T. H., III, Harnessing the power of plastics: nanostructured polymer systems in lithium-ion batteries. *ACS Energy Letters* **2017,** *2* (8), 1919-1936.
3. Chen, Y.; Kang, Y.; Zhao, Y.; Wang, L.; Liu, K.; Li, Y.; Liang, Z.; He, X.; Li, X.; Tavajohi, N.; Li, B., A review of lithium-ion battery safety concerns: the issue, strategies, and testing standards. *Journal of Energy Chemistry* **2021,** *59*, 83-99.
4. Hallinan, D. T., Jr.; Balsara, N. P., Polymer electrolytes. *Annual Review of Materials Research* **2013,** *43*, 503-525.
5. Trahey, L.; Brushett, F. R.; Balsara, N. P.; Ceder, G.; Cheng, L.; Chiang, Y. M.; Hahn, N. T.; Ingram, B. J.; Minteer, S. D.; Moore, J. S.; Mueller, K. T.; Nazar, L. F.; Persson, K. A.; Siegel, D. J.; Xu, K.; Zavadil, K. R.; Srinivasan, V.; Crabtree, G. W., Energy storage emerging: a perspective from the Joint Center for Energy Storage Research. *Proceedings of the National Academy of Sciences of the United States of America* **2020,** *117* (23), 12550-12557.
6. Morris, M. A.; Gartner, T. E., III; Epps, T. H., III, Tuning block polymer structure, properties, and processability for the design of efficient nanostructured materials systems. *Macromolecular Chemistry and Physics* **2017,** *218* (5), 1600513.
7. Christie, D.; Register, R. A.; Priestley, R. D., Direct measurement of the local glass transition in self-assembled copolymers with nanometer resolution. *ACS Central Science* **2018,** *4* (4), 504-511.
8. Ganesan, V.; Pyramitsyn, V.; Bertoni, C.; Shah, M., Mechanisms underlying ion transport in lamellar block copolymer membranes. *ACS Macro Letters* **2012,** *1* (4), 513-518.
9. Sharon, D.; Bennington, P.; Dolejsi, M.; Webb, M. A.; Dong, B. X.; de Pablo, J. J.; Nealey, P. F.; Patel, S. N., Intrinsic ion transport properties of block copolymer electrolytes. *ACS Nano* **2020,** *14* (7), 8902-8914.
10. Sharon, D.; Bennington, P.; Webb, M. A.; Deng, C. T.; de Pablo, J. J.; Patel, S. N.; Nealey, P. F., Molecular level differences in ionic solvation and transport behavior in ethylene oxide-based homopolymer and block copolymer electrolytes. *Journal of the American Chemical Society* **2021,** *143* (8), 3180-3190.
11. Sethuraman, V.; Pryamitsyn, V.; Ganesan, V., Influence of molecular weight and degree of segregation on local segmental dynamics of ordered block polymers. *Journal of Polymer Science, Part B: Polymer Physics* **2016,** *54* (9), 859-864.
12. Ketkar, P. M.; Epps, T. H., III, Nanostructured block polymer electrolytes: tailoring self-assembly to unlock the potential in lithium-ion batteries. *Accounts of Chemical Research* **2021,** *54* (23), 4342-4353.
13. Kuan, W.-F.; Remy, R.; Mackay, M. E.; Epps, T. H., III, Controlled ionic conductivity *via* tapered block polymer electrolytes. *RSC Advances* **2015,** *5* (17), 12597-12604.
14. Ketkar, P. M.; Shen, K.-H.; Fan, M.; Hall, L. M.; Epps, T. H., III, Quantifying the effects of monomer segment distributions on ion transport in tapered block polymer electrolytes. *Macromolecules* **2021,** *54* (16), 7590-7602.

15. Luo, M.; Brown, J. R.; Remy, R. A.; Scott, D. M.; Mackay, M. E.; Hall, L. M.; Epps, T. H., III, Determination of interfacial mixing in tapered block polymer thin films: experimental and theoretical investigations. *Macromolecules* **2016,** *49* (14), 5213-5222.
16. Morris, M. A.; Sung, S. H.; Ketkar, P. M.; Dura, J. A.; Nieuwendaal, R. C.; Epps, T. H., III, Enhanced conductivity *via* homopolymer-rich pathways in block polymer-blended electrolytes. *Macromolecules* **2019,** *52* (24), 9682-9692.
17. Gartner, T. E., III; Morris, M. A.; Shelton, C. K.; Dura, J. A.; Epps, T. H., III, Quantifying lithium salt and polymer density distributions in nanostructured ion-conducting block polymers. *Macromolecules* **2018,** *51* (5), 1917-1926.
18. Gilbert, J. B.; Luo, M.; Shelton, C. K.; Rubner, M. F.; Cohen, R. E.; Epps, T. H., III, Determination of lithium-ion distributions in nanostructured block polymer electrolyte thin films by X-ray photoelectron spectroscopy depth profiling. *ACS Nano* **2015,** *9* (1), 512-520.
19. Gomez, E. D.; Panday, A.; Feng, E. H.; Chen, V.; Stone, G. M.; Minor, A. M.; Kisielowski, C.; Downing, K. H.; Borodin, O.; Smith, G. D.; Balsara, N. P., Effect of ion distribution on conductivity of block copolymer electrolytes. *Nano Letters* **2009,** *9* (3), 1212-1216.
20. Nguyen, H. K.; Liang, X.; Ito, M.; Nakajima, K., Direct mapping of nanoscale viscoelastic dynamics at nanofiller/polymer interfaces. *Macromolecules* **2018,** *51* (15), 6085-6091.
21. Christie, D.; Register, R. A.; Priestley, R. D., Role of chain connectivity across an interface on the dynamics of a nanostructured block copolymer. *Physical Review Letters* **2018,** *121* (24), 247801.
22. Sethuraman, V.; Ganesan, V., Segmental dynamics in lamellar phases of tapered copolymers. *Soft Matter* **2016,** *12* (37), 7818-7823.
23. Ketkar, P. M.; Shen, K.-H.; Hall, L. M.; Epps, T. H., III, Charging toward improved lithium-ion polymer electrolytes: exploiting synergistic experimental and computational approaches to facilitate materials design. *Molecular Systems Design & Engineering* **2019,** *4* (2), 223-238.
24. Chu, W.; Qin, J.; de Pablo, J. J., Ion distribution in microphase-separated copolymers with periodic dielectric permittivity. *Macromolecules* **2018,** *51* (5), 1986-1991.
25. Webb, M. A.; Savoie, B. M.; Wang, Z.-G.; Miller, T. F., III, Chemically specific dynamic bond percolation model for ion transport in polymer electrolytes. *Macromolecules* **2015,** *48* (19), 7346-7358.
26. Webb, M. A.; Yamamoto, U.; Savoie, B. M.; Wang, Z.-G.; Miller, T. F., III, Globally suppressed dynamics in ion-doped polymers. *ACS Macro Letters* **2018,** *7* (6), 734-738.
27. Glaser, J.; Qin, J.; Medapuram, P.; Morse, D. C., Collective and single-chain correlations in disordered melts of symmetric diblock copolymers: Quantitative comparison of simulations and theory. *Macromolecules* **2014,** *47* (2), 851-869.
28. Sivia, D. S., *Elementary scattering theory for X-ray and neutron users*. Oxford University Press: New York, 2011.
29. Michler, G. H., *Electron Microscopy of Polymers*. Springer: Heidelberg, Germany, 2008.
30. Russell, T. P., Changes in polystyrene and poly(methyl methacrylate) interactions with isotopic substitution. *Macromolecules* **1993,** *26* (21), 5819-5819.
31. Harton, S. E.; Stevie, F. A.; Zhu, Z. M.; Ade, H., Changes in thermodynamic interactions at highly immiscible polymer/polymer interfaces due to deuterium labeling. *Journal of Physical Chemistry B* **2006,** *110* (22), 10602-10605.

32. Goswami, M.; Iyiola, O. O.; Lu, W.; Hong, K. L.; Zolnierczuk, P.; Stingaciu, L.-R.; Heller, W. T.; Taleb, O.; Sumpter, B. G.; Hallinan, D. T., Jr., Understanding interfacial block copolymer structure and dynamics. *Macromolecules* **2023,** *56* (3), 762-771.
33. Nakamura, I.; Wang, Z.-G., Salt-doped block copolymers: ion distribution, domain spacing and effective χ parameter. *Soft Matter* **2012,** *8* (36), 9356-9367.
34. Sharick, S.; Koski, J.; Riggleman, R. A.; Winey, K. I., Isolating the effect of molecular weight on ion transport of non-ionic diblock copolymer/ionic liquid mixtures. *Macromolecules* **2016,** *49* (6), 2245-2256.
35. Shen, K.-H.; Fan, M.; Hall, L. M., Molecular dynamics simulations of ion-containing polymers using generic coarse-grained models. *Macromolecules* **2021,** *54* (5), 2031–2052.
36. Wheatle, B. K.; Keith, J. R.; Mogurampelly, S.; Lynd, N. A.; Ganesan, V., Influence of dielectric constant on ionic transport in polyether-based electrolytes. *ACS Macro Letters* **2017,** *6*, 1362-1367.
37. Lodge, T. P.; McLeish, T. C. B., Self-concentrations and effective glass transition temperatures in polymer blends. *Macromolecules* **2000,** *33* (14), 5278-5284.
38. Timachova, K.; Watanabe, H.; Balsara, N. P., Effect of molecular weight and salt concentration on ion transport and the transference number in polymer electrolytes. *Macromolecules* **2015,** *48* (21), 7882-7888.
39. Heijboer, J., Secondary loss peaks in glassy amorphous polymers. *International Journal of Polymeric Materials* **1977,** *6* (1-2), 11-37.
40. Boyer, R. F., Dependence of mechanical properties on molecular motion in polymers. *Polymer Engineering and Science* **1968,** *8* (3), 161-185.
41. Kenny, J. C.; McBrierty, V. J.; Rigbi, Z.; Douglass, D. C., Carbon black filled natural rubber. 1. Structural investigations. *Macromolecules* **1991,** *24* (2), 436-443.
42. Shen, K.-H.; Hall, L. M., Effects of ion size and dielectric constant on ion transport and transference number in polymer electrolytes. *Macromolecules* **2020,** *53* (22), 10086-10096.
43. Young, W.-S.; Epps, T. H., III, Ionic conductivities of block copolymer electrolytes with various conducting pathways: sample preparation and processing considerations. *Macromolecules* **2012,** *45* (11), 4689-4697.
44. Coote, J. P.; Kinsey, T.; Street, D. P.; Kilbey, S. M., II; Sangoro, J. R.; Stein, G. E., Surface-induced ordering depresses through-film ionic conductivity in lamellar block copolymer electrolytes. *ACS Macro Letters* **2020,** *9* (4), 565-570.
45. Wang, X.; Chintapalli, M.; Newstein, M. C.; Balsara, N. P.; Garetz, B. A., Characterization of a block copolymer with a wide distribution of grain sizes. *Macromolecules* **2016,** *49* (21), 8198-8208.
46. Burns, A. B.; Christie, D.; Mulhearn, W. D.; Register, R. A., Estimating the segregation strength of microphase-separated diblock copolymers from the interfacial width. *Journal of Polymer Science Part B-Polymer Physics* **2019,** *57* (14), 932-940.
47. Patterson, A. L.; Yu, B. H.; Danielsen, S. P. O.; Davidson, E. C.; Fredrickson, G. H.; Segalman, R. A., Monomer sequence effects on interfacial width and mixing in self-assembled diblock copolymers. *Macromolecules* **2020,** *53* (9), 3262-3272.
48. Anastasiadis, S. H.; Russell, T. P.; Satija, S. K.; Majkrzak, C. F., The morphology of symmetric diblock copolymers as revealed by neutron reflectivity. *The Journal of Chemical Physics* **1990,** *92* (9), 5677-5691.

49. Morèse-Séguéla, B.; St-Jacques, M.; Renaud, J. M.; Prud'homme, J., Microphase separation in low molecular weight styrene-isoprene diblock copolymers studied by DSC and ^{13}C NMR. *Macromolecules* **1980,** *13*, 100-106.
50. Pietra, N. F.; Korovich, A. G.; Ketkar, P. M.; Epps, T. H., III; Madsen, L. A., Role of intra-domain heterogeneity on ion and polymer dynamics in block polymer electrolytes: Investigating interfacial mobility and ion-specific dynamics and transport. **(In review)**.
51. Ma, P. Y.; Mirmira, P.; Amanchukwu, C. V., Effect of building block connectivity and ion solvation on electrochemical stability and ionic conductivity in novel fluoroether electrolytes. *ACS Central Science* **2021,** *7* (7), 1232-1244.
52. Singh, M.; Odusanya, O.; Wilmes, G. M.; Eitouni, H. B.; Gomez, E. D.; Patel, A. J.; Chen, V. L.; Park, M. J.; Fragouli, P.; Iatrou, H.; Hadjichristidis, N.; Cookson, D.; Balsara, N. P., Effect of molecular weight on the mechanical and electrical properties of block copolymer electrolytes. *Macromolecules* **2007,** *40* (13), 4578-4585.
53. Panday, A.; Mullin, S.; Gomez, E. D.; Wanakule, N.; Chen, V. L.; Hexemer, A.; Pople, J.; Balsara, N. P., Effect of molecular weight and salt concentration on conductivity of block copolymer electrolytes. *Macromolecules* **2009,** *42* (13), 4632-4637.
54. Amanchukwu, C. V.; Gunnarsdottir, A. B.; Choudhury, S.; Newlove, T. L.; Magusin, P.; Bao, Z. A.; Grey, C. P., Understanding lithium-ion dynamics in single-ion and salt-in-polymer perfluoropolyethers and polyethyleneglycol electrolytes using solid-state NMR. *Macromolecules* **2023,** *56* (10), 3650-3659.
55. Deng, C. T.; Webb, M. A.; Bennington, P.; Sharon, D.; Nealey, P. F.; Patel, S. N.; de Pablo, J. J., Role of molecular architecture on ion transport in ethylene oxide-based polymer electrolytes. *Macromolecules* **2021,** *54* (5), 2266-2276.
56. Bennington, P.; Deng, C. T.; Sharon, D.; Webb, M. A.; de Pablo, J. J.; Nealey, P. F.; Patel, S. N., Role of solvation site segmental dynamics on ion transport in ethylene-oxide based side-chain polymer electrolytes. *Journal of Materials Chemistry A* **2021,** *9* (15), 9937-9951.
57. Liu, J. C.; Pickett, P. D.; Park, B.; Upadhyay, S. P.; Orski, S. V.; Schaefer, J. L., Non-solvating, side-chain polymer electrolytes as lithium single-ion conductors: synthesis and ion transport characterization. *Polymer Chemistry* **2020,** *11* (2), 461-471.
58. Heimenz, P. C.; Lodge, T. P., *Polymer Chemistry*. 2nd ed.; CRC Press: Boca Raton, Florida, 2007.
59. Epps, T. H., III; Bailey, T. S.; Waletzko, R.; Bates, F. S., Phase behavior and block sequence effects in lithium perchlorate-doped poly(isoprene-b-styrene-b-ethylene oxide) and poly(styrene-b-isoprene-b-ethylene oxide) triblock copolymers. *Macromolecules* **2003,** *36* (8), 2873-2881.
60. Zhu, L.; Cheng, S. Z. D.; Calhoun, B. H.; Ge, Q.; Quirk, R. P.; Thomas, E. L.; Hsiao, B. S.; Yeh, F.; Lotz, B., Phase structures and morphologies determined by self-organization, vitrification, and crystallization: confined crystallization in an ordered lamellar phase of PEO-*b*-PS diblock copolymer. *Polymer* **2001,** *42* (13), 5829-5839.
61. Kuan, W.-F.; Reed, E. H.; Nguyen, N. A.; Mackay, M. E.; Epps, T. H., III, Using tapered interfaces to manipulate nanoscale morphologies in ion-doped block polymers. *MRS Communications* **2015,** *5* (2), 251-256.
62. Brown, J. R.; Seo, Y. M.; Sides, S. W.; Hall, L. M., Unique phase behavior of inverse tapered block copolymers: self consistent field theory and molecular dynamics simulations. *Macromolecules* **2017,** *50* (14), 5619-5626.

63. Seo, Y.; Brown, J. R.; Hall, L. M., Diffusion of selective penetrants in interfacially modified block copolymers from molecular dynamics simulations. *ACS Macro Letters* **2017,** *6* (4), 375-380.
64. Patterson, A. L.; Danielsen, S. P. O.; Yu, B. H.; Davidson, E. C.; Fredrickson, G. H.; Segalman, R. A., Sequence effects on block copolymer self-assembly through tuning chain conformation and segregation strength utilizing sequence-defined polypeptoids. *Macromolecules* **2019,** *52* (3), 1277-1286.
65. Schneider, H. A., Glass transition behavior of compatible polymer blends. *Polymer* **1989,** *30* (5), 771-779.
66. Yuan, R.; Teran, A. A.; Gurevitch, I.; Mullin, S. A.; Wanakule, N. S.; Balsara, N. P., Ionic conductivity of low molecular weight block copolymer electrolytes. *Macromolecules* **2013,** *46* (3), 914-921.
67. Allen, F. H.; Kennard, O.; Watson, D. G., Tables of bond lengths determined by X-ray and neutron diffraction. Part I. Bond lengths in organic compounds. *Journal of the Chemical Society, Perkin Transactions 2* **1987**, S1-S19.
68. Patnode, W.; Scheiber, W. J., The density, thermal expansion, vapor pressure, and refractive index of styrene, and the density and thermal expansion of polystyrene. *Journal of the American Chemical Society* **1939,** *61* (12), 3449-3451.
69. Evans, C. M.; Kim, S.; Roth, C. B.; Priestley, R. D.; Broadbelt, L. J.; Torkelson, J. M., Role of neighboring domains in determining the magnitude and direction of T_g-confinement effects in binary, immiscible polymer systems. *Polymer* **2015,** *80*, 180-187.
70. Dalle-Ferrier, C.; Kisliuk, A.; Hong, L.; Carini, G.; D'Angelo, G.; Alba-Simionesco, C.; Novikov, V. N.; Sokolov, A. P., Why many polymers are so fragile: a new perspective. *Journal of Chemical Physics* **2016,** *145* (15), 154901.
71. Sokolov, A. P.; Novikov, V. N.; Ding, Y., Why many polymers are so fragile. *Journal of Physics-Condensed Matter* **2007,** *19* (20), 205116.
72. Becher, M.; Becker, S.; Hecht, L.; Vogel, M., From local to diffusive dynamics in polymer electrolytes: NMR studies on coupling of polymer and ion dynamics across length and time scales. *Macromolecules* **2019,** *52* (23), 9128-9139.
73. Loo, W. S.; Faraone, A.; Grundy, L. S.; Gao, K. W.; Balsara, N. P., Polymer dynamics in block copolymer electrolytes detected by neutron spin echo. *ACS Macro Letters* **2020,** *9* (5), 639-645.
74. Sax, J.; Ottino, J. M., Modeling of transport of small molecules in polymer blends: Application of effective medium theory. *Polymer Engineering and Science* **1983,** *23* (3), 165-176.
75. Seki, S.; Susan, A. B. H.; Kaneko, T.; Tokuda, H.; Noda, A.; Watanabe, M., Distinct difference in ionic transport behavior in polymer electrolytes depending on the matrix polymers and incorporated salts. *Journal of Physical Chemistry B* **2005,** *109* (9), 3886-3892.
76. Timachova, K.; Chintapalli, M.; Olson, K. R.; Mecham, S. J.; DeSimone, J. M.; Balsara, N. P., Mechanism of ion transport in perfluoropolyether electrolytes with a lithium salt. *Soft Matter* **2017,** *13* (32), 5389-5396.
77. France-Lanord, A.; Wang, Y. M.; Xie, T.; Johnson, J. A.; Shao-Horn, Y.; Grossman, J. C., Effect of chemical variations in the structure of poly(ethylene oxide)-based polymers on lithium transport in concentrated electrolytes. *Chemistry of Materials* **2020,** *32* (1), 121-126.

78. Jung, H. Y.; Mandal, P.; Jo, G.; Kim, O.; Kim, M.; Kwak, K.; Park, M. J., Modulating ion transport and self-assembly of polymer electrolytes via end-group chemistry. *Macromolecules* **2017,** *50*, 3224-3233.
79. Steinrück, H. G.; Takacs, C. J.; Kim, H.-K.; Mackanic, D. G.; Holladay, B.; Cao, C. T.; Narayanan, S.; Dufresne, E. M.; Chushkin, Y.; Ruta, B.; Zontone, F.; Will, J.; Borodin, O.; Sinha, S. K.; Srinivasan, V.; Toney, M. F., Concentration and velocity profiles in a polymeric lithium-ion battery electrolyte. *Energy & Environmental Science* **2020,** *13* (11), 4312-4321.
80. Chen, Y. X.; Lee, E. M. Y.; Gil, P. S.; Ma, P. Y.; Amanchukwu, C. V.; de Pablo, J. J., Molecular engineering of fluoroether electrolytes for lithium metal batteries. *Molecular Systems Design & Engineering* **2023,** *8* (2), 195-206.